

A Novel Dynamic Graph-Based Computational Model for Predicting Salivary Gland Branching Morphogenesis

Nimit Dhulekar, Lauren Bange, Abhirami Baskaran,
Daniel Yuan, Basak Oztan, Bülent Yener
CS Dept., Rensselaer Polytechnic Institute, Troy, NY, USA
dhulena@cs.rpi.edu, bangel@alum.rpi.edu, baskaa@rpi.edu,
yuand@rpi.edu, oztanb@cs.rpi.edu, yener@cs.rpi.edu

Shayoni Ray, Melinda Larsen
Biological Sciences Department
University at Albany, SUNY
Albany, NY, USA
sray@albany.edu, mlarsen@albany.edu

Abstract—In this paper, we introduce a biologically motivated dynamic graph-based growth model to describe and predict the stages of cleft formation during the process of branching morphogenesis in the submandibular mouse gland (SMG) from 3 hrs after embryonic day $E12$ to 8 hrs after embryonic day $E12$, which can be considered as $E12.5$. Branching morphogenesis is the process by which many mammalian exocrine and endocrine glands undergo significant morphological transformations, from a primary bud to an adult organ. Although many studies have investigated the cellular and molecular mechanisms driving branching morphogenesis, it is not clear how the shape changes that are inherent to establishing organ structure are produced. Using morphological features extracted from sequential images of SMG organ cultures we were able to develop a dynamic graph-based predictive model that is able to mimic the process of cleft formation and predict the final state. In addition, we compare our model to a state-of-the-art Glazier-Graner-Hogeweg (GGH) simulative tool, and demonstrate that the dynamic graph-based predictive model has comparable accuracy in modeling growth of clefts across SMG developmental stages, as well as faster convergence to the target SMG morphology.

Keywords—morphogenesis, cell behavior, epithelial, mathematical model, cell-graph, dynamic graph growth

I. INTRODUCTION

Branching morphogenesis is the process of development of many mammalian exocrine and endocrine glands such as the lungs, kidney, pancreas, mammary, and salivary glands [1]. The organization of a branched morphology maximizes the total area of contact between the metabolic exchange surfaces and the surrounding environment while minimizing the total volume of the organ. This allows for an efficient exchange of gases, nutrients, metabolites, and wastes.

During branching morphogenesis of the mouse submandibular gland (SMG), the morphology of the gland undergoes significant transformation [2]. For purpose of illustration, Fig. 1 shows three stages of growth of a submandibular mouse gland (SMG) starting from a primary bud in Fig. 1a, where small clefts, or indentations, have initiated on the surface of the primary bud. In Fig. 1b clefts, or indentations, have appeared in the surface of the bud and have started to undergo cleft progression to separate the primary bud into multiple smaller buds. Cleft progression includes a cellular contraction as well as cellular proliferation that result in bud outgrowth [3]. Clefts ultimately cease progressing and begin to widen at their base, as seen in the left-most bud in Fig. 1c that shows the SMG at a much advanced stage. This widening is followed by outgrowth of the cells at the base of the clefts to form ducts. Once the new buds are fully formed, cleft formation begins on the new buds, and occurs reiteratively throughout development to create the ramified structure of the adult organ.

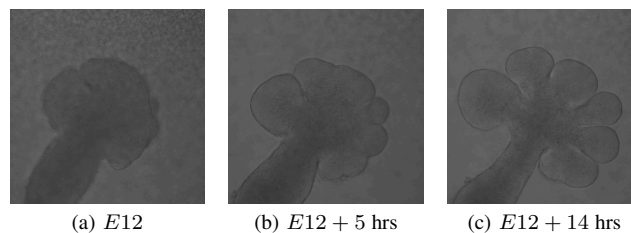


Figure 1: Three stages of branching morphogenesis in SMG demonstrating progressively deeper clefts and bud outgrowth. In (a), multiple nascent clefts are visible on a single large bud, which deepen in (b) and begin to form buds. By image (c), some clefts have terminated, and the gland has been separated into distinct buds.

Branching morphogenesis requires an understanding of the molecular mechanisms regulating epithelium-mesenchyme interactions during development of the glands. The process is highly dynamic, involving interactions between multiple participating cells and molecules. These interactions cannot be completely understood using conventional cellular and molecular biology methods alone, which has increased interest in this area of systems biology [4], [5]. Initial systems approaches to understanding morphogenesis were based on the Turing morphogenesis model [6] and focused on pattern formation and its applications to morphogenesis. The Eden model [7] was a competing method that grows the tissue by selecting a periphery cell with at least one empty nearest neighbor, and then with equal probability choosing and occupying one of its empty nearest neighbors. Since then, many advanced mathematical models based on differential-algebraic equations, flux balance analysis, and stochastic algorithms, have been utilized to develop a better understanding of morphogenesis [8]–[10]. Simulation tools have also made it possible to analyze various cellular behaviors that are difficult to examine *in vivo* [11].

In this paper, we introduce a dynamic graph-based growth technique to predict branching morphogenesis of the SMG as a function of initial gland morphology, cell proliferation rate, cleft progression rate, and cell-cell adhesion. The SMG is widely used to study branching morphogenesis [12], and shares common mechanisms with the other types of salivary glands [13] and other branching organs [2]. In the current study, we focus on developing a predictive and descriptive model for the process of cleft formation in the first round of branching morphogenesis, which initiates

in the SMG at *E12*, starting from the initiation of clefts and proceeding through cleft progression. Our model terminates prior to the apparent widening of clefts that occurs during ductal formation and does not address the second or subsequent rounds of branching that occur as the gland continues to develop. Note that branching morphogenesis progresses beyond this stage (embryonic day *E13*); however, we are limiting our focus in this paper to the earliest stage of morphogenesis and excluding the processes of duct formation and hollowing of the structure [14].

Graph-based models are commonly used to model highly complex events at various scales with multiple participants. In particular, biological networks have benefitted from the use of graph-theoretical concepts that have been used to model protein-protein interactions [15], [16], disease progression [17], and neuronal connectivity [18]. Our proposed model builds upon our earlier work on histopathological image analysis [19], tissue modeling [21], and characterization of branching morphogenesis at embryonic day *E13* [22], at cellular and tissue scales using a graph-theoretical method called *cell-graphs*. Cell-graphs are unweighted and undirected graphs where the cell nuclei are represented by graph nodes, and interactions between cells are represented by edges. Cell-graphs enable us to assess the spatial uniformity, connectedness, and compactness at multiple scales. When a cell undergoes mitosis, the daughter cell inherits not only the genetic characteristics of the parent cell but also the local topological characteristics of its neighborhood [23]. In our proposed model, this similarity is enforced via the local structural properties of cell-graphs that maintain consistency in the topology of the SMG throughout the development stages. The SMG also maintains a smooth boundary during the growth stages, and we utilize a function of the locations of the nodes in the cell-graph to encode this smoothness into our model.

To evaluate the efficacy of our model, we extract morphological features that characterize developmental stages of the SMG branching morphogenesis. Our results closely mimic the observed developmental stages. In addition, we compare to a state-of-the-art simulative model based on how well the dynamic graph model represents the process of cleft formation observable in SMG developmental stages, and the computational time complexity.

The rest of this paper is organized as follows: in Section II, we present the materials and methods; in particular, the proposed SMG branching morphogenesis dynamic growth model is described in detail in Section II-C. We present our experimental results and a discussion in Section III and finally, in Section IV, we present conclusions.

II. MATERIALS AND METHODS

In this section, we first introduce the time-lapse data that forms our ground truth in Section II-A. Next, we present features for the characterization of the SMG morphology in Section II-B, and finally, our dynamic graph-based SMG branching morphogenesis prediction model is presented in detail in Section II-C.

A. Acquisition of Data

Our ground truth is a time-lapse image set of an embryonic day *E12* SMG that was treated with disperse, and had the mesenchyme physically removed by microdissection, as described in [24].

The epithelial rudiment was grown in Matrigel (1:1 dilution in DMEM/F12 growth media) supplemented with 100U/ml penicillin, 100 mg/ml streptomycin, 50 mg/ml transferrin, 150 mg/ml ascorbic acid, 20 ng/ml epidermal growth factor (EGF), and 100 ng/ml fibroblast growth factor (FGF). The gland was imaged using time-lapse microscopy at 200X magnification using a Zeiss 510 Meta confocal microscope. 87 images were captured as $7\mu\text{m}$ sections at 10 minute intervals using the 488 nm laser to capture a near DIC image. Images were captured at a 512×512 pixel resolution using a scan speed of 8 in line averaging mode. These images were visually inspected to identify the morphological changes in progressing clefts that occurs in the period from 3 hrs to 8 hrs after *E12*.

To obtain nuclear information regarding cell distribution, cell proliferation rates, and cell morphologies, we used separate *ex vivo* data set. Intact *E12* SMGs were cultured for 2 hours, 8 hours, 12 hours, and 24 hours and pulsed for 2 hours with Click-iT Edu. Following this process SMGs were fixed and permeabilized in 4% PFA. Labeled DNA was detected using Click-iT EdU Alexa Flour 647 kit (Invitrogen). Following EdU detection, glands were blocked and immunostained with antibody recognizing E-cadherin (1:100) and Cy5-conjugated Donkey F(ab)2 secondary antibody (1:100, Jackson ImmunoResearch Lab) to detect the epithelial area. Total nuclei were detected using SYBR Green I (Invitrogen) counter staining. Immunostained glands were imaged using a laser scanning confocal microscope (Zeiss 510 Meta) at 20x (Plan APO/0.75 NA) using identical settings for all samples. Multiple images overlapping each other by approximately 10% were acquired at the center of each explant (depth direction) such that the entire explant was imaged.

B. Characterization of the SMG morphology

In the following subsections we describe the initial image processing steps to segment the SMG regions from the time-lapse image set (Section II-B1), identify clefts in the SMG (Section II-B2), and characterize the SMG using morphological features (Section II-B3).

1) *Preliminary Image Processing*: In order to characterize the SMG morphology, the SMG regions in the time-lapse data set need to be segmented. Due to the significantly low contrast and high noise of these images, it was difficult to automatically segment the SMG regions with high accuracy. Therefore, we manually segmented the SMG regions using ImageJ [25]. Since SMG growth is characterized by bud outgrowth and cleft deepening, the stem regions were also eliminated during the manual segmentation.

2) *Initial Cleft Detection*: A critical step in modeling SMG branching morphogenesis is the detection and characterization of clefts as they form and deepen. The SMG boundary is comprised of alternating bud and cleft regions, with clefts as narrow valley-shaped formations that separate growing buds. For the purpose of illustration Fig. 2 shows the progression stages of a typical cleft. Narrowing and deepening of the cleft can be observed from Fig. 2(a) to (c) as branching morphogenesis progresses.

We characterize the cleft regions using their center and two extrema points as illustrated in Fig. 3a. The cleft center is the deepest point of the cleft, with the walls extending on either side of the surface normal at the cleft center. The cleft extrema points determine the extent of the cleft; the bud region starts

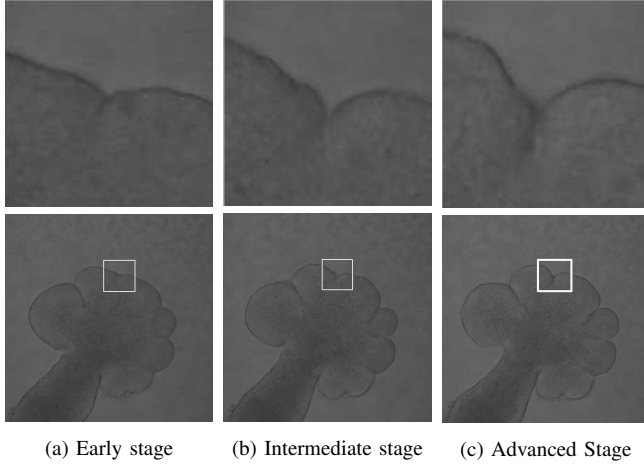


Figure 2: Stages of cleft formation during branching morphogenesis illustrating (a) early, (b) intermediate and (c) advanced stages. Images in the top row are enlarged segments of the images shown in the bottom row wherein other clefts at different progressive stages can also be seen.

beyond these points. Automated detection of these key points is carried out as follows: first we compute the angles at each point with its eighth neighboring points on either side along the SMG boundary. These extrema correspond to not only the potential cleft centers but also the peaks of boundary irregularities. Next, the peak points are eliminated using the signed area of the triangle formed by the cleft center, and two of its immediate neighbors along the boundary ordered in clockwise direction. This is obtained as $\begin{vmatrix} x_{c-1} & y_{c-1} & 1 \\ x_c & y_c & 1 \\ x_{c+1} & y_{c+1} & 1 \end{vmatrix}$, where (x_c, y_c) , (x_{c-1}, y_{c-1}) , and (x_{c+1}, y_{c+1}) represent the horizontal and vertical coordinates of the candidate point and its previous and next neighbors along the boundary, respectively. This expression is positive for clefts and negative for peaks. After the peaks are eliminated, we identify the cleft extrema points using the mean-squared error (MSE) between the best-fit line and SMG boundary points on each side of the potential cleft centers. For each side, the algorithm progresses from the cleft center including a neighboring boundary node, and fitting a line between the center and the set of points in consideration. When the MSE exceeds a threshold the node is labeled as a cleft extrema. We set a dynamic threshold for the MSE, varying between 10 and $40\mu m$ which is computed as a function of cleft depth obtained from fitting a convex hull around the SMG. A convex hull is the smallest convex polygon that fully contains the SMG without progressing into concavities such as the cleft regions. The cleft depth is calculated as the shortest distance from the cleft center to the line joining points on either side of it that lie on the convex hull.

In order to eliminate boundary irregularities or nascent clefts, we exploit the cleft depth and spanning angle as illustrated for a sample cleft in Fig. 3a. Cleft depth is taken as the Euclidean distance from the cleft center to the line segment joining the two extrema points and the spanning angle is formed by the two line segments joining the extrema points to the center. We considered clefts that have a

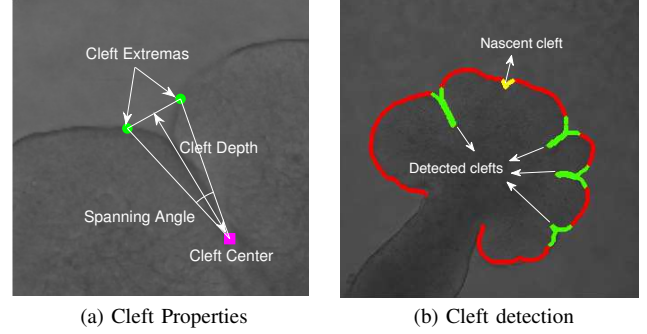


Figure 3: Characterization of clefts. Subfigure (a) shows extrema and cleft center points that characterize the cleft. Spanning angle and cleft depth are calculated from these points as illustrated. Subfigure (b) shows an intermediate stage SMG where the detected and nascent clefts are marked in green and yellow, respectively.

depth less than $22\mu m$ as boundary irregularities or nascent clefts and eliminated them from our model. In our analysis we observe that the spanning angles of the detected clefts were between 8° and 125° . Figure 3b shows a ground truth image with detected clefts highlighted in green and nascent clefts in yellow. Note that the detected clefts have varying depths and spanning angles that are representative of the cleft developmental stages illustrated in Fig. 2.

The time-lapse data from a stereotypical gland was partitioned into three developmental stages of SMG morphogenesis based on the number of clefts detected in each image by our algorithm. *Early stage* glands were defined as those that have three clefts detected that progress from 3 hrs after E12 to 4 hrs 40 mins after E12. From that point *intermediate stage* glands that have four detected clefts progress until 6 hrs after E12 and finally *advanced stage* glands that have five detected clefts progress until 8 hrs after E12. While this stereotypical gland was assumed to be the “ground truth” data for this study, minor variability can be detected in independent samples in terms of how many and what quality of clefts are present at any given time of development.

3) SMG Morphological Features: Visual inspection of the time-lapse data reveals significant differences in morphology. To quantitatively capture these changes, we extract six morphological features, area, perimeter, eccentricity, solidity, and box-count dimension, described next. Figure 4 shows plots of these features, as well as a linear regression to indicate general trends.

Area and perimeter are counts of pixels within the SMG region and on the boundary of the SMG region, respectively. Both increase with time as the SMG grows, as seen in Figs. 4a and 4b. Isoperimetric quotient and eccentricity are measurements that quantify the elongation of the SMG. The isoperimetric quotient is the ratio of the area of the SMG region to the square of its perimeter, and which decreases as the SMG becomes more elliptical, as shown in Figure 4c. Eccentricity is a measure of the circularity of the ellipse fitted to the SMG that has the same second-moments as the SMG. It is defined as the ratio of the distance between the foci of the ellipse and its major axis length. Eccentricity increases as the SMG becomes more elongated throughout the growth stages, visible in Fig. 4d. Solidity is computed as the ratio of areas of the SMG region to its convex hull. Because deepening clefts cause a relative

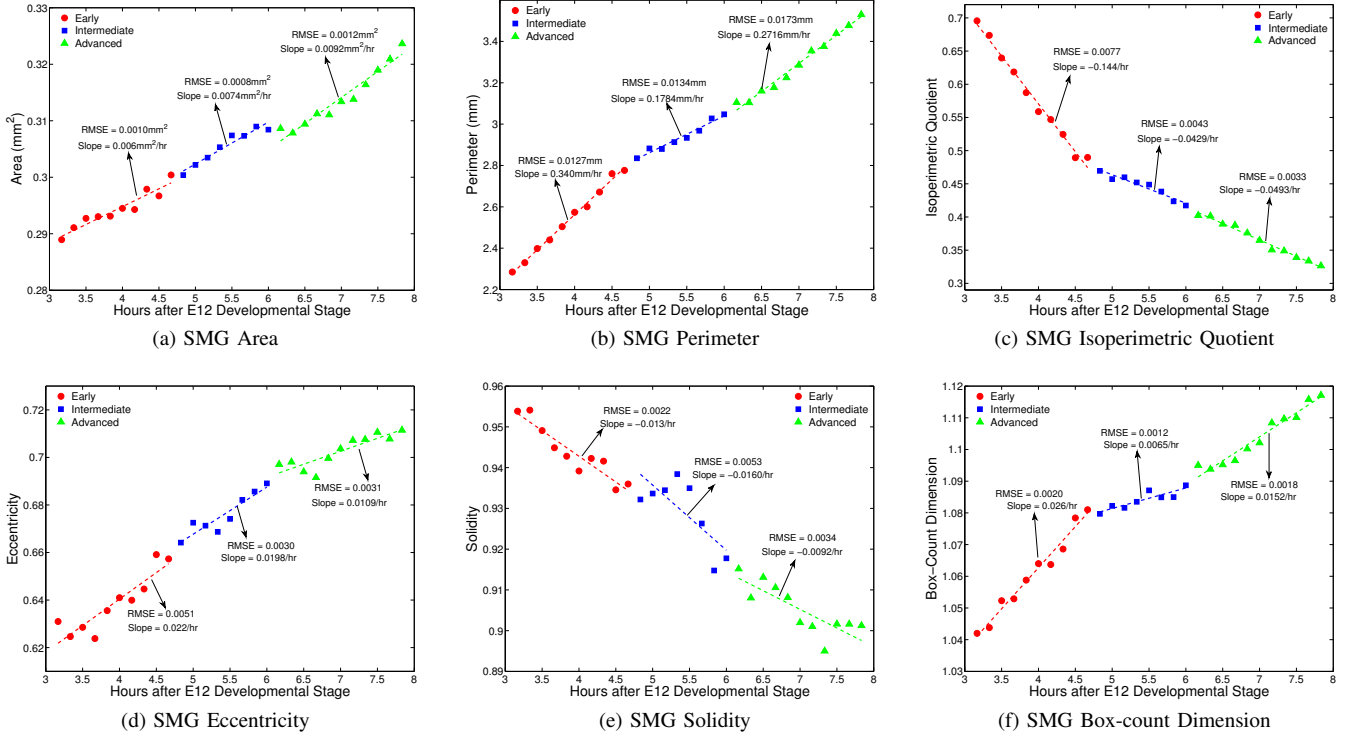


Figure 4: Features characterizing the morphology of SMG developmental stages. Area, perimeter, isoperimetric quotient, eccentricity, solidity, and box-count dimension of the three stages are shown in (a)–(f), respectively. The trends in each feature are indicated with the best-fit lines (dashed lines), the fitting root-mean-square errors, and best-fit line slopes within the plots.

decrease in the SMG region’s area but do not affect the convex hull, solidity decreases over time, confirmed in Fig. 4e. The box-count dimension is a measure of a shape’s space-filling capacity. The method overlays the SMG region with boxes of increasing size, recording the number of boxes required to cover the boundary. We use the slope of the best-fit line in log-log space with least MSE to the vector containing box-count dimension values for square boxes of size $2^n \times 2^n$ where n varies from 0 to 9. Cleft deepening is expected to increase the box-count dimension, and is indeed observed in Fig 4f.

C. Biologically-driven Dynamic Graph-Based Growth Model for Prediction of Branching Morphogenesis

The dynamic graph growth technique is an extension of static cell-graphs to capture and model time-varying data. A static cell-graph $G = (V, E)$ consists of a set of nodes V representing cell nuclei, and a set of edges E representing the interactions between cells. An edge is inserted into E when the pair-wise Euclidean distance between two nuclei in set V is less than a pre-determined threshold.

In addition to the initial gland morphology and cell locations, our model incorporates cellular proliferation and cleft progression rates. We assume cells to be circular in shape, and size is approximated by the diameter. Here, the initial image in each developmental stage was used for gland morphology; information from the *ex vivo* data set was used to determine the cell proliferation rate and diameter. The cleft progression rate was determined from the time-lapse data

by the cleft detection algorithm described in Section II-B2. Since the time-lapse data does not provide nuclear information, and the *ex vivo* data consists of different tissue samples, starting cell locations were approximated by a uniform grid overlaid on the SMG. This approximation was based on cell density measurements made on the *ex vivo* data set. At each growth step, cells are divided into two populations based on the distance from the gland boundary, namely internal and periphery. A subset of both cell populations are chosen to undergo a proliferation attempt. For the internal cells that are selected for proliferation, we compute the shortest distance to the boundary of the gland (not including the cleft region) and find the periphery cell closest to that boundary point.

To model cell proliferation we impose additional assumptions that build upon the Eden model, which considers all cells to be identical, and permits growth only at the gland boundary where the mesenchymal nutrient medium is accessible [7]. Creation of new cells in the cleft region is disallowed to prevent the cleft from closing, but the SMG is allowed to grow around the cleft. This inhibition of cell proliferation in the cleft region is equivalent to the replacement of the epithelial cell-cell junctions with the cell-extracellular matrix (ECM) junctions where fibronectin (FN) translocates along SMG epithelial cells into nascent clefts and keeps them in their current state [24]. To model increase in cleft depth, we use the cleft progression rate obtained from the time-lapse data to determine the distance that the cleft needs to be extended at every iteration of the algorithm. The cleft progression

rate changes over time, and thus we model the length by which to extend the cleft depth as a function of time. We move the cleft center by this distance along the surface normal in the opposite direction to the cleft extrema. We use a cubic spline interpolation between the cleft center and its -2 and $+2$ neighbors along the SMG boundary to form the extended cleft. Restricting cell proliferation in the cleft region as well as increasing cleft depth causes the cleft to narrow and deepen, both characteristics of progressive cleft formation. Table I lists biological processes and properties, and the corresponding mechanisms to handle them in our model. We run separate simulations for the three stages of SMG

Biology	Dynamic Graph Model	GGH Model
Gland Structure	Graph Geometry	Effective Energy
Mitosis	New Node Creation	Mitosis
Cell-cell Adhesion	Graph Links (Edges)	Contact Energy
	Link Length	FPP
Cell Volume	Min. Link Length	Cell Area
Cell Surface Area	Not Included	Cell Perimeter

Table I: Biological processes and properties, and their corresponding interpretations in our model, and the state-of-art simulative model used for comparison in Section III.

development (early, intermediate, and advanced) starting with the initial image of each set. The steps involved in each iteration of our dynamic growth algorithm are as follows:

- 1) *Creation of new nodes*: The cell proliferation rate is calculated from the *ex vivo* data set as a percentage of the total cell population. Periphery nodes are probabilistically chosen to undergo mitosis, creating new daughter nodes. These daughter nodes are placed outside the initial gland boundary in a region within 20° of the surface normal at a minimum distance of one cell diameter, but less than the specified maximum edge length. Five possible candidate daughter nodes satisfying these spatial and angular constraints are chosen, and the daughter node with the shortest Euclidean distance to the parent node is selected as the optimal daughter node. The local structural features assess the spatial uniformity (clustering coefficients C,D,E), connectedness (degree, closeness, betweenness), and compactness (nearest neighbor distance, mean edge length) of the cell-graph. Please refer [22] for further details about local structural features. To model bud outgrowth in a local region and prevent spikes in the gland boundary, we distribute the extension distances to the neighbors of the parent node.
- 2) *Maintaining boundary smoothness*: After all daughter nodes have been created, the spatial orientation of nodes is used to create a smoother gland boundary. The smoothness algorithm is based on the intuition that if daughter nodes are aligned similarly to the parent nodes, then smoothness will be maintained when the daughter nodes are included into the boundary. This is accomplished by minimizing the quantity $|\phi'_i - \phi_i|$, where ϕ_i is the angle $\angle p_{i-1}p_i p_{i+1}$, and ϕ'_i is the angle $\angle p_{i-1}p'_i p_{i+1}$, as shown in Fig. 5. The previous and next nodes p_{i-1} and p_{i+1} , respectively, are fixed, and the position of the daughter node p'_i is varied along the line segment $p_i p'_i$. This process is repeated from the second

till the $(n - 1)$ th daughter node, keeping the first and n th daughter nodes fixed.

- 3) *Updating the gland boundary*: Use a interpolating cubic spline curve to join the daughter nodes to the gland boundary. If the distance between the current and next daughter nodes is greater than a threshold, we connect the current daughter node to the $+3$ neighbor of the parent node along the SMG boundary.
- 4) *Terminating the algorithm*: The simulation is run for 20 iterations, after which the terminal step is calculated. We compute the morphological feature vector and compare it to the feature vectors of the first and last images in the particular set (3, 4, or 5 clefts) of the ground truth using a weighted Euclidean distance. The weights for the features are determined from the ground truth using singular value decomposition [26]. The iteration that has the minimum distance to the last image is considered as the terminal stage.

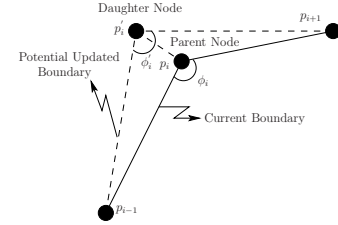


Figure 5: Smoothing of SMG boundary in dynamic graph model. Spatial positions of parent nodes in the current boundary are used to identify optimal location for daughter nodes.

III. RESULTS AND DISCUSSION

We follow the methodology explained in the previous section and generate SMG branching morphogenesis states using the proposed dynamic graph-based growth model starting from the image of the *E12* gland grown for 3 hrs where initiated clefts are detected. We were able to mimic the developmental stages of the ground truth data based on the number of clefts as identified by our cleft detection algorithm (Section II-B2). Figure 6 (a)–(c) shows early, intermediate, and advanced stages of growth generated by our model. The figure shows a gradual increase in the area and perimeter, and deepening of the clefts over time. We also compare our results against a well-known simulative model, the Glazier-Graner-Hogeweg (GGH) model. Note that in simulative models the target configurations are specified along with the initial configurations, and therefore there is a high likelihood of reproducing the target configurations. In contrast to a simulative model, for a predictive model only the initial configuration is specified. In this section, we first describe the GGH model briefly, and then present comparative results between the models and against the ground truth data.

A. Glazier-Graner-Hogeweg (GGH) model

To measure the efficacy of the proposed dynamic graph-based model, we compare it against the GGH model, also known as the Cellular Potts model. This simulative model has been successfully used in a variety of biological modeling applications such as tumor growth and organ development [27], [28]. The GGH model treats cells as a cluster of sites on a fixed lattice. Interactions between these cells and their adjacent lattice sites impose an energy penalty,

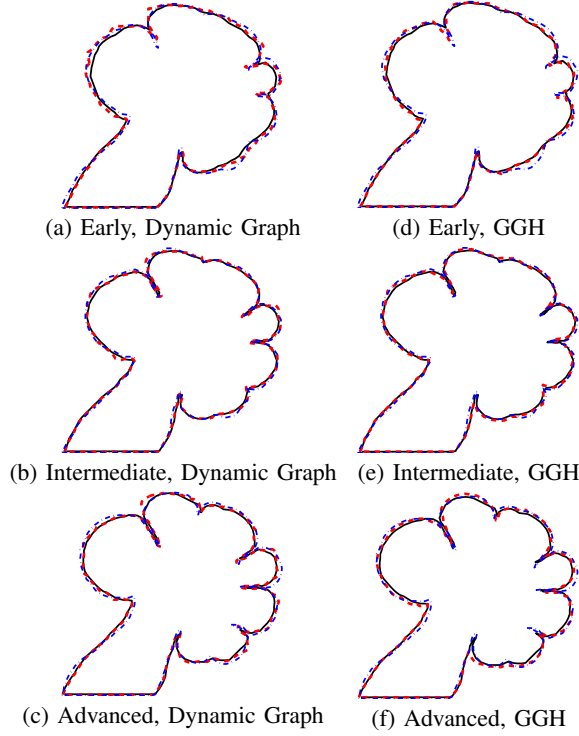


Figure 6: Gland boundaries for the (a)–(c) dynamic graph model and (d)–(f) the GGH model for early (*top*), intermediate (*middle*), and advanced (*bottom*) stages, respectively. The black solid curve represents the ground truth used as the initial configuration; the blue dash-dotted curve represents the final ground truth image of the stage, and the red dotted curve represents the final configuration of the model at termination.

and the sum of these interaction energies is the effective energy, also known as the *Hamiltonian*. Each energy penalty represents a biological constraint or interaction between cells, and the system attempts to minimize the effective energy through repeated Monte Carlo Simulation (MCS) steps. At each MCS step, lattice sites are chosen at random, and an attempt is made to copy it to a neighboring lattice site. The acceptance rate is determined by the change in the system’s effective energy; changes lowering the effective energy are always accepted, while those increasing the effective energy are accepted with a probability based on the energy difference and a motility constant [29]. We run multiple simulations for the three SMG developmental stages beginning with the initial image from each set. The simulation is run for 2000 MCS steps being initialized with the images described in Section II-B2, after which the terminal step is calculated.

In the GGH simulation, development of the SMG was modeled via contact energy and focal point plasticity (FPP) interactions, and cells were given an area and perimeter constraint. Additionally, a module for simulating mitosis was used to grow the model gland. The biological relevance of these conditions are compared in Table I, and described as follows:

Contact Energy simulates differential adhesion between cells of different types. It examines neighboring lattice sites belonging to different cells, and assigns an energy penalty to each type of

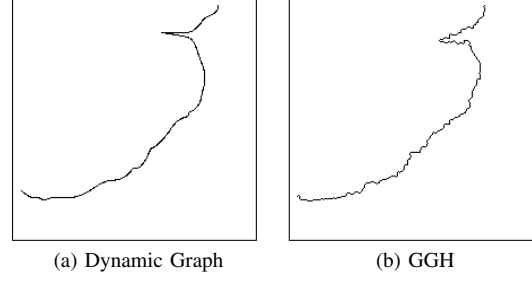


Figure 7: (a) and (b) show enlarged views from the dynamic graph and GGH model simulations shown in red dotted curves in Figs. 6(b) and (e), respectively. Note that the SMG boundary in the dynamic graph model is significantly smoother than the GGH model simulation.

interaction. Lower contact energy is specified between cleft cells and the ECM, to encourage deepening of clefts.

Focal Point Plasticity simulates large-scale attractive and repulsive forces between cells arising from adhesion interactions. It creates links between cells and sets a target distance between their centroids and an energy penalty based on how far the actual distance deviates from this target. Cells making up the opposite sides of the cleft increase their target distance as the simulation progresses; cleft and border cells are also linked to maintain an orderly gland boundary.

Cell Area is the 2D representation of cell volume. Biological cells attempt to grow to and maintain a certain volume.

Cell Perimeter is the 2D representation of the surface area. Like volume, this is a physical constraint imposed by the cell’s finite amount of membrane, limiting their shape.

Mitosis occurs in a manner similar to biological cell division; GGH cells chosen for mitosis have their target area and perimeter increased until their actual area has doubled, at which point they are bifurcated along a random axis. The lattice sites of each half are assigned to daughter cells, which also inherit all of the original properties of the parent cell. Mitosis is not tied to the effective energy.

We used an open-source GGH environment called CompuCell 3D (<http://www.compuCell3d.org>). A 6×6 grid was overlaid on the image, and pixels were assigned to GGH cells. Five cell types were defined – two cleft types representing opposite sides of the cleft, bud region, ECM, and a single non-changing stem region. Acceptable parameters were found via parametric search, and the gland configuration was saved every 10 MCS steps. Figure 6 (d)–(f) shows the growth of the gland boundary from the initial to final configuration for 3, 4, and 5 clefts.

B. Comparative Analysis

In order to determine the stage of the process of cleft formation in branching morphogenesis in the resulting predictions and simulations, we capture the morphology of the SMG for each of the three cleft progression stages using the features explained in Section II-B3. We computed the z-scores for each feature vector for both models with respect to the averaged ground truth feature vector for the corresponding cleft developmental stage. This enables us to determine the number of iterations that belong to each cleft developmental stage. Since termination is calculated

based on all six features individual features values may deviate from the ground truth. In addition, we compare the mean and standard deviation of individual features for the dynamic graph model against the ground truth and GGH model, as seen in Fig. 8.

SMG Developmental Stages	Early	Intermediate	Advanced
Ground Truth	2.04 ± 1.18	2.13 ± 0.91	2.19 ± 0.86
Dynamic Graph Model	2.16 ± 0.91	2.94 ± 0.63	2.25 ± 0.44
GGH Model	2.10 ± 0.54	3.05 ± 0.49	2.38 ± 0.46

Table II: Mean and standard deviation of the ground truth, dynamic graph model, and GGH model from the average ground truth feature vector for each of the three SMG developmental stages.

Both models demonstrate an increase in area and perimeter over the three stages, which conforms to the ground truth. For the early stage, multiple clefts are forming in the SMG which reduces the rate of growth of the area (Fig. 4(a)). Even though the dynamic graph model employs cleft deepening, it grows at a constant rate, and thus displays a higher area than the ground truth. GGH grows the clefts at a fast rate, and thus reaches equilibrium soon; this prevents it from reaching the final area of the ground truth. Differences in the isoperimetric quotient are directly proportional to those in area and perimeter, and also conform to the ground truth values. Average eccentricity (Fig. 8(d)) is slightly lower for both the dynamic graph and GGH models. In the former, this is a consequence of our smoothness constraints whereas in the latter, it results from the omnidirectional growth of the SMG, as well as the tendency for SMG cells to adhere due to the contact energy penalty with the ECM. There is minimal variation in solidity, as seen in Fig. 8(e). Solidity for both models decreases over time as a consequence of clefting, which matches the ground truth. The smoothness constraint applied to the dynamic graph model also reduces the box-count dimension; in contrast, the more jagged boundary of the GGH model results in a higher box-count dimension. The difference is also clearly visible in the enlarged visual representations of the two models, in Fig. 7. Table II shows the mean and standard deviation of the ground truth, dynamic graph model, and the GGH model from the average ground truth feature vector for the three SMG developmental stages. This table presents a view of how well the feature vectors match the particular SMG developmental stage. The high standard deviation of the ground truth is a consequence of variable cleft progression rates in all three stages. The mean distance for the feature vector of the dynamic graph model is closer to the ground truth than the GGH model for 2 out of the 3 stages.

One of the main strengths of our model lies in its fast computational time. In order to compare the computational time complexities of our model, we ran experiments against the GGH simulation on a 2.4 GHz Intel Core 2 Duo processor with 4 GB RAM. On average, our dynamic graph-based model takes 12 iterations for a total time of $180.4 \text{ sec} \pm 12 \text{ sec}$ to predict the developmental stages, whereas GGH takes about 860 MCS steps to reach the target SMG morphology in a time of $27 \text{ min} \pm 35 \text{ sec}$, resulting in a speed-up factor of approximately 9. The large volume of data generated by the GGH model also requires significant post-processing time and

disk space. Also, the GGH model considers cellular-level detail and thus is more complex than our model, and hence it is not surprising that our model takes less execution time.

IV. CONCLUSION

We introduce a biologically motivated dynamic graph-based growth model to describe and predict the stages of cleft formation during submandibular salivary gland branching morphogenesis. By using the initial morphology of the gland, our model predicts the growth of the SMG preserving local structural properties between the cells and the smoothness of the gland surface. Our results indicate that we closely mimicked the tissue-level morphological changes during cleft formation process in the developmental stages of the SMG branching morphogenesis. In addition, we compared our results against a well-known simulative model and demonstrated that our results are comparable and converge significantly faster to the target configuration. Some future directions for our model involve including dynamic cell movement information [24] and generating clefts dynamically; the latter would be valuable in modeling more advanced stages of branching morphogenesis.

ACKNOWLEDGMENT

The authors would like to thank Dr. James A. Glazier and his research group members Dr. Abbas Shirinifard and Dr. Srividhya Jeyaraman at Indiana University, Bloomington, IN for discussions, suggestions, and help with the use of GGH model for SMG branching morphogenesis. This work was supported by a grant from the NIH to Melinda Larsen and Bülent Yener (R01 DE019244).

REFERENCES

- [1] J. Davies, *Branching Morphogenesis*, ser. Molecular Biology Intelligence Unit. Birkhäuser, 2006.
- [2] M. Affolter, S. Bellusci, N. Itoh, B. Shilo, J. Thiery, and Z. Werb, "Tube or not tube: remodeling epithelial tissues by branching morphogenesis," *Developmental Cell*, vol. 4, no. 1, pp. 11–18, 2003.
- [3] W. P. Daley, E. M. Gervais, S. W. Centanni, K. M. Gulfo, D. A. Nelson, and M. Larsen, "Rock1-directed basement membrane positioning coordinates epithelial tissue polarity," *Development*, vol. 139, no. 2, pp. 411–422, 2012.
- [4] E. Klipp, W. Liebermeister, C. Wierling, A. Kowald, H. Lehrach, and R. Herwig, *Systems Biology: A Textbook*, 1st ed. Wiley-VCH, Aug. 2009.
- [5] D. Hartmann and T. Miura, "Modelling in vitro lung branching morphogenesis during development," *Journal of Theoretical Biology*, vol. 242, no. 4, pp. 862–872, Oct. 2006.
- [6] A. M. Turing, "The chemical basis of morphogenesis," *Philosophical Transactions of the Royal Society (B)*, vol. 237, no. 641, pp. 37–72, August 1952.
- [7] M. Eden, "A two-dimensional growth process," *Berkeley Symposium on Mathematical Statistics and Probability*, vol. 4, pp. 223–239, 1961.
- [8] H. Meinhardt, "Pattern formation in biology: a comparison of models and experiments," *Reports on Progress in Physics*, vol. 55, no. 6, pp. 797–849, 1992.
- [9] M. Markus, D. Böhm, and M. Schmick, "Simulation of vessel morphogenesis using cellular automata," *Mathematical Biosciences*, vol. 156, no. 1-2, pp. 191–206, 1999.

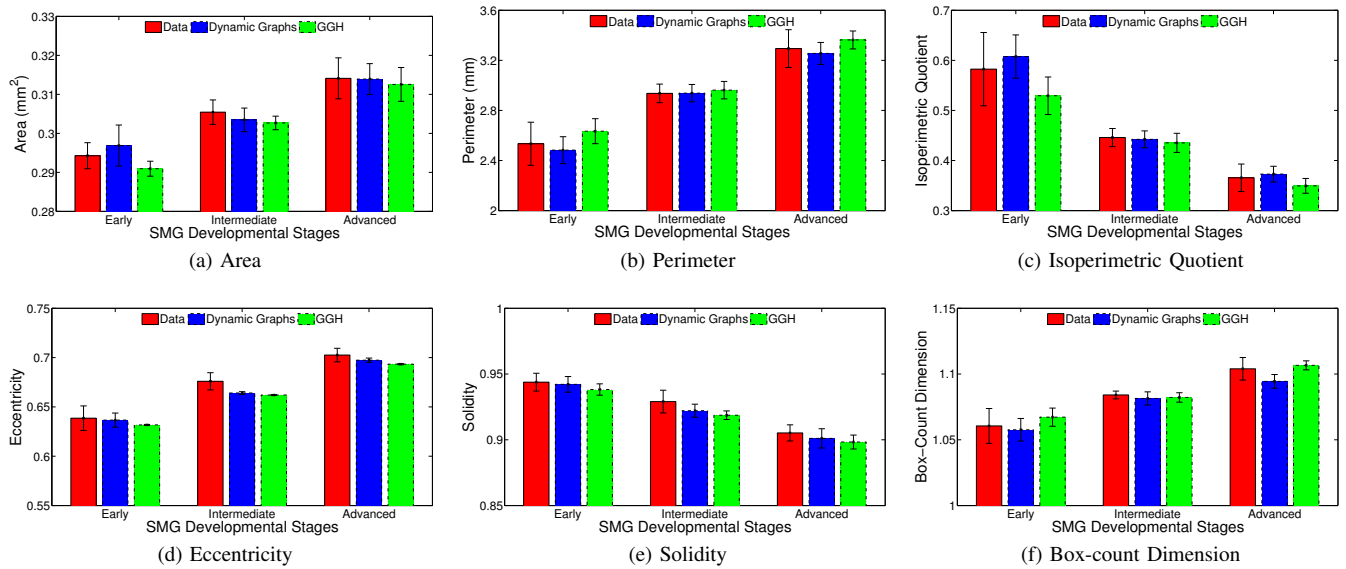


Figure 8: Comparison of SMG morphological features between developmental stages of ground truth (red), dynamic graph growth model (blue), and the GGH simulation (green). The features are (a) area, (b) perimeter, (c) isoperimetric quotient, (d) eccentricity, (e) solidity, and (f) box-count dimension. Note that the scale has been magnified to emphasize minute differences.

- [10] L. Forest and J. Demongeot, "A general formalism for tissue morphogenesis based on cellular dynamics and control system interactions," *Acta Biotheoretica*, vol. 56, no. 1, pp. 51–74, June 2008.
- [11] Y. Setty, D. Dalfó, D. Z. Korta, E. J. A. Hubbard, and H. Kugler, "A model of stem cell population dynamics: in-silico analysis and in-vivo validation," *Development*, vol. 139, pp. 47–56, January 2012.
- [12] B. S. Spooner and N. K. Wessells, "An analysis of salivary gland morphogenesis: role of cytoplasmic microfilaments and microtubules," *Developmental Biology*, vol. 27, pp. 38–54, 1972.
- [13] P. C. Denny, W. D. Ball, and R. S. Redman, "Salivary glands: a paradigm for diversity of gland development," *Critical Reviews in Oral Biology and Medicine*, vol. 8, pp. 51–75, 1997.
- [14] A. S. Tucker, "Salivary gland development," *Seminars in cell developmental biology*, vol. 18, no. 2, pp. 237–244, 2007.
- [15] H. Jeong, S. P. Mason, A. L. Barabási, and Z. N. Oltvai, "Lethality and centrality in protein networks," *Nature*, vol. 411, no. 6833, pp. 41–42, May 2001.
- [16] A. Wagner, "The yeast protein interaction network evolves rapidly and contains few redundant duplicate genes," *Molecular Biology and Evolution*, vol. 18, no. 7, pp. 1283–1292, Jul. 2001.
- [17] A.-L. Barabási, "Network Medicine — From Obesity to the "Diseasome"," *New England Journal of Medicine*, vol. 357, no. 4, pp. 404–407, Jul. 2007.
- [18] D. J. Watts and S. H. Strogatz, "Collective dynamics of 'small-world' networks," *Nature*, vol. 393, no. 6684, pp. 440–442, Jun. 1998.
- [19] C. Gunduz, B. Yener, and S. H. Gultekin, "The cell graphs of cancer," *Bioinformatics*, vol. 20, no. 1, pp. 145–151, Jan. 2004.
- [20] C. Bilgin, P. Bullough, G. E. Plopper, and B. Yener, "Ecm-aware cell-graph mining for bone tissue modeling and classification," *Data Min. Knowl. Discov.*, vol. 20, no. 3, pp. 416–438, May 2010.
- [21] C. Bilgin, A. W. Lund, A. Can, G. E. Plopper, and B. Yener, "Quantification of three-dimensional cell-mediated collagen re-modeling using graph theory," *PLoS ONE*, vol. 5, no. 9, 2010.
- [22] C. Bilgin, S. Ray, B. Baydil, W. P. Daley, M. Larsen, and B. Yener, "Multiscale feature analysis of salivary gland branching morphogenesis," *PLoS ONE*, vol. 7, no. 3, 03 2012.
- [23] W. Becker, L. J. Kleinsmith, J. Hardin, and G. P. Bertoni, *The world of the cell*. Benjamin/Cummings Pub. Co., 1986.
- [24] M. Larsen, C. Wei, and K. M. Yamada, "Cell and fibronectin dynamics during branching morphogenesis," *Journal of Cell Science*, vol. 119, pp. 3376–3384, August 2006.
- [25] M. D. Abramoff, P. J. Magalhaes, and S. J. Ram, "Image processing with ImageJ," *Biophotonics International*, vol. 11, no. 7, pp. 36–42, 2004.
- [26] L. McKeen-Polizzotti, K. Henderson, B. Oztan, C. Bilgin, B. Yener, and G. E. Plopper, "Quantitative metric profiles capture three-dimensional temporospatial architecture to discriminate cellular functional states," *BMC Medical Imaging*, vol. 11, no. 11, 2011.
- [27] N. J. Poplawski, A. Shirinifard, U. Agero, J. S. Gens, M. Swat, and J. A. Glazier, "Front instabilities and invasiveness of simulated 3d avascular tumors," *Plos One*, vol. 5, no. 5, May 2010.
- [28] D. E. Larson, R. I. Johnson, M. Swat, J. B. Cordero, J. A. Glazier, and R. L. Cagan, "Computer simulation of cellular patterning within the *Drosophila* pupal eye," *Plos Computational Biology*, vol. 6, no. 7, July 2010.
- [29] F. Graner and J. A. Glazier, "Simulation of biological cell sorting using a two-dimensional extended potts model," *Physical review letters*, vol. 69, no. 13, pp. 2013–2016, September 1992.